Geomechanics and Engineering, *Vol. 17, No. 1 (2019) 97-107*
DOI: https://doi.org/10.12989/gae.2019.17.1.097

An improved collapse analysis mechanism for the face stability of shield tunnel in layered soils

Guang-hui Chen[a], Jin-feng Zou[*] and Ze-hang Qian[b]

School of Civil Engineering, Central South University, No.22, Shaoshan South Road, Central South University Railway Campus, Changsha, Hunan Province, People's Republic of China

(Received October 13, 2017, Revised December 10, 2018, Accepted December 11, 2018)

Abstract. Based on the results of Han *et al.* (2016), in the failure zone ahead of the tunnel face it can be obviously identified that a shear failure band occurs in the lower part and a pressure arch happens at the upper part, which was often neglected in analyzing the face stability of shield tunnel. In order to better describe the collapse failure feature of the tunnel face, a new improved failure mechanism is proposed to evaluate the face stability of shield tunnel excavated in layered soils in the framework of limit analysis by using spatial discretization technique and linear interpolation method in this study. The developed failure mechanism is composed of two parts: i) the rotational failure mechanism denoting the shear failure band and ii) a uniformly distributed force denoting the pressure arch effect. Followed by the comparison between the results of critical face pressures provided by the developed model and those by the existing works, which indicates that the new developed failure mechanism provides comparatively reasonable results.

Keywords: face stability; shield tunnel; layered soils; limit analysis; pressure arch effect

1. Introduction

With the development of urbanization, more and more shallow tunnels are emerging. For shallow tunnels, there are two key problems to be solved: i) ground deformation and ii) stability of tunnel faces. This study only focus on the later, in which the tunnel face would collapse when the support pressure acting on the tunnel face is not sufficient. Experiments, numerical simulations and analytical approaches had been proposed by some authors to investigate the face stability of the shield tunnel in cohesionless or cohesion-frictional soils, and solve many engineering problems (Chambon and Corté 1994, Anagnostou and Kovári 1996, Kirsch 2010, Indinger *et al.* 2011, Schuller and Schweiger 2002, Chen *et al.* 2015, Oreste and Dias 2012, Mollon *et al.* 2009, Pan and Dias 2016b, Mollon *et al.* 2011, Pan and Dias 2016a, Zou and Zhang 2019c, Zou *et al.* 2019d). The researches progress of these methods are presented respectively below.

Experiment methods, especially small-scale laboratory centrifuge tests, are widely used to analyze the face stability of shield tunnel and the failure feature of the corresponding surrounding soils. For example, Chambon and Corté (1994) investigated a series of practical effects, especially tunnel unlined length, on the face stability of the tunnel in purely frictional soils by using centrifugal-model tests. The results indicated that the extent of failure mechanism varied with the tunnel unlined length. In order to assess the quality of the existing failure mechanisms, Kirsch (2010) conducted a small-scale model tests of single gravity in undrained condition. The results showed that the failure features of surrounding soils did not change during the failure process for the presence of a much more diffuse failure zone in the condition of loose samples. Indinger *et al.* (2011) conducted an investigation of stability of tunnel face on a small-scale tunnel model in geotechnical centrifuge. The results indicated that the contours of shear strain obviously existed in crossed layer, whereas not in cover layer. However, it needs to be mentioned that these experimental methods are not able to give a deterministic result due to the design schemes of these experimental tests may have a great influence on the results, and the reproducibility of the model tests has not been confirmed. In addition, with the development of finite difference techniques, numerical simulations are increasingly being used to derive the limit support pressures and the features of collapse failure models. For example, Schuller and Schweiger (2002), based on the Multilaminate Models, conducted a constitutive model to analyze the practical problem of tunnel excavation, for example staged excavation sequence, on the tunnel face stability. The results indicated that the failure mechanism, especially shear banding, is caused by the development of plastic shear strains. Chen *et al.* (2013) discussed the collapse failure feature and critical support pressure for various cover depths by employing the finite difference program, FLAC3D. The results showed that the support pressure of tunnel face firstly decreased to the critical support pressure and then increased to the residual support pressure with the increasing of the horizontal

∗Corresponding author, Professor
E-mail: zoujinfeng_csu@163.com
[a]Postgraduate Student
E-mail: 15700731178@163.com
[b]Postgraduate Student
E-mail: 15200806569@163.com

 ISSN: 2005-307X (Print), 2092-6219 (Online)

displacement in front of the tunnel face. Moreover, the results also demonstrated the presence of soil arching in the upper part of the collapse failure zone. However, the numerical simulation methods are time-consuming and usually requires a larger number of input variables, some of which should be estimated or assumed if not available at hand.

For the analytical approaches, the limit equilibrium methods are widely used to analyze the stability of the tunnel face in the early years based on various failure models, e.g., the wedge model (Horn 1961), wedge-prism model (Anagnostou and Kovári 1996, Chen *et al.* 2013) and triangular base prism model (Oreste and Dias 2012). For example, Krause (1987) analyzed the stability of tunnel face by assuming that the failure zone was a half sphere, a half circle or a quarter circle. Anagnostou and Kovári (1996) utilized the wedge failure model introduced by Horn (1961) to evaluate the required limit support pressures in homogeneous soils. Normalized diagrams are further provided to assess the stability of tunnel face. In addition, Chen *et al.* (2013) proposed an improved 3D wedge-prism model considering the height of the prism and the effect of soil arching to access the tunnel face stability in the cohesionless ground. For its simplicity, limit equilibrium methods are extensively used in the practical engineering to investigate the limit support pressure of tunnel face. However, it lacks of consideration of the stress-strain relationship of the soil, which is the factor that must be fulfilled for a complete solution proposed by Chen (1975). Furthermore, it needs some assumptions relating to internal forces to meet relevant requirements that are not easily justified in the limit equilibrium method and the results obtained from limit equilibrium method are neither a strict lower- nor upper-bound solution. In accordance with the limit equilibrium method, the limit analysis methods have a more rigorous theoretical basis and can provide better solutions, which were widely applied to access the tunnel face stability by many researchers recently based on various failure models, e.g., the horn model (Subrin and Wong 2002), multi-block model (Mollon *et al.* 2009) and rotational failure model (Mollon *et al.* 2011, Pan and Dias 2016b, Zou *et al.* 2019a). For example, Leca and Dormieux (1990) proposed the rigid conical blocks failure model to analyze the upper- and lower-bound solutions of the limit support pressures in dry Mohr-Coulomb. Mollon *et al.* (2009) proposed an improved multi-block collapse mechanism based on Leca and Dormieux (1990). In addition, an interesting blow-out mechanism was conducted by this study. Zhang *et al.* (2015), based on the work of Soubra (2000), developed a new analytical model which was composed of five truncated cones denoting the shear failure band and a uniformly distributed force acting on the top face of the fifth truncated cones denoting soil arching effect in multilayered cohesive-frictional soils by using upper-bound limit analysis methods. The results indicated that the failure feature of the crossed and cover layer is more consistent with the results obtained from experiments and numerical simulation (Broere 2001, Vermeer *et al.* 2002). By using spatial discretization and "point by point" technique, Mollon *et al.* (2011) firstly proposed the rotational failure mechanism considering the failure zone of the whole circular tunnel face which is a great improvement in the solution of the face stability. Compared with previous classic failure mechanisms, the shape of the shear failure band of collapse rotational failure mechanism was more consistent with the phenomena observed in experiments and numerical simulation (Chen *et al.* 2011, Chen *et al.* 2013). In addition, the effects of seepage force, reinforcement, layered soils and nonlinearity failure rule on the face stability of tunnel were investigated by Khezri *et al.* (2016), Mollon *et al.* (2010), Pan and Dias (2016b), Zou *et al.* (2019a), Yang and Yan (2015) and Yang *et al.* (2016) in the framework of limit analysis methods. A distinct advantage of the mentioned analytical methods including the limit analysis and limit equilibrium methods lie in that the developed formulas can provide meaningful physical insight into the governing parameters and also offer a direct design for practical tunnel engineers with less time-consuming.

This paper, based on the two features (shear failure band occurs in the lower part and pressure arch effect happens at the upper part) reported by Han *et al.* (2016), proposes a new collapse failure mechanism to analyze stability of tunnel face and obtain the limit support pressures by using kinematic approach of limit analysis theory in layered soils condition. The developed mechanism is composed of the rotational failure mechanism adjacent to the tunnel face denoting the shear failure band and a uniformly distributed force acting on the top of the rotational failure mechanism denoting the pressure arch effect. And the distributed force is calculated by Terzaghi earth theory. Then the limit support pressures obtained by this paper are validated with those from Han *et al.* (2016) and Senent and Jimenze (2015).

2. Introduction of the new collapse failure mechanism

With the application of "point by point" and spatial discretization technique, Mollon *et al.* (2011) proposed an advanced collapse rotational failure mechanism (see Fig. 1(a)) which is proved to make a great improvement in the analysis of tunnel face stability. However, from the results of the experiments and numerical methods, it is easy to identify the two main failure characteristics of soil in front of the tunnel face, that is, shear failure band occurs in the lower part and pressure arch effect happens at the upper part. In order to better represent the aforementioned failure feature of soil in front of tunnel face, a new collapse failure mechanism is proposed by the combination of the earth pressure theory and the kinematic approach of limit analysis to investigate the face stability of a tunnel with the diameter of D and buried depth of C driven in single layer. It can be seen from Fig. 1(b) that the new collapse failure mechanism is composed of the rotational failure mechanism adjacent to the tunnel face which represents the shear failure band and a uniformly distributed force acting on the top of the rotational failure mechanism which represents the pressure arch effect. Note that only the part adjacent to the tunnel face of the rotational failure mechanism obtained from Mollon *et al.* (2011) is preserved (see Fig. 1). The uniformly distributed force acting on the top of the rotational failure mechanism is calculated by the Terzaghi

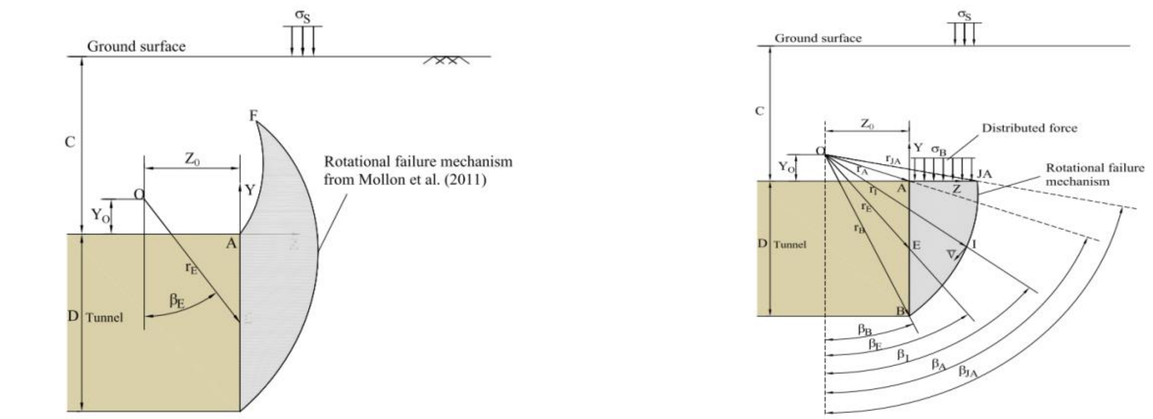

(a) Rotational failure mechanism (Mollon *et al.* 2011) (b) The new failure mechanism

Fig. 1 Longitudinal section of (a) rotational failure mechanism from Mollon *et al.* (2011) and (b) the new failure mechanism

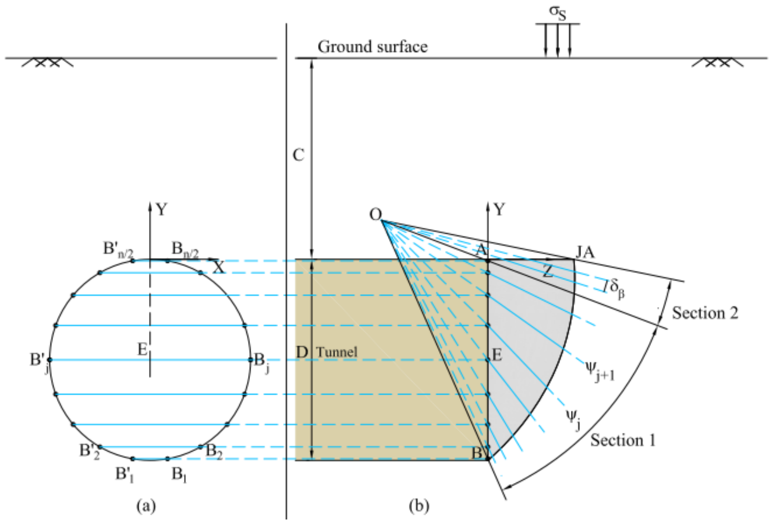

Fig. 2 View of (a) discretization of tunnel face and (b) construction plans in Section 1 and Section 2

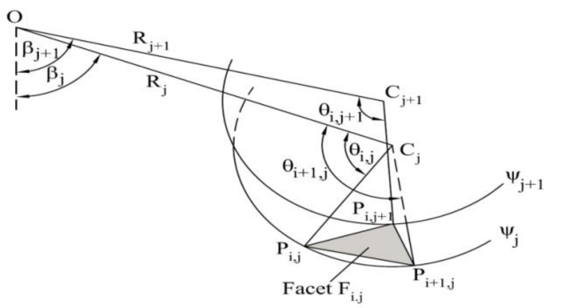

Fig. 3 The produce of the generation of point $P_{i,j+1}$ from points $P_{i,j}$ and $P_{i+1,j}$

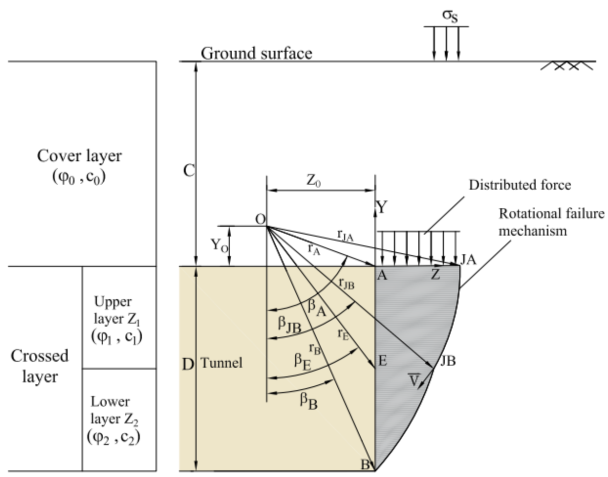

Fig. 4 Longitudinal section of the new failure mechanism in two layers with location of the intersection in crossed layer

earth pressure theory which was extensively applied in Anagnostou (2012), Zou *et al.* (2019b), Anagnostou and Perazzelli (2013), Broere (2001) and Tang *et al.* (2014).

2.1 Generation of rotational failure mechanism

Fig. 1(b) shows that the rotational failure mechanism adjacent to the tunnel face rotates with a uniform angular velocity ω around a horizontal X-axis passing through point O. Consequently, the velocity vector of any point I can be denoted as R_I (see Fig. 1(b)), which indicates that the velocity vector is independent of the X coordination. Note that the longitude section of the rotational failure

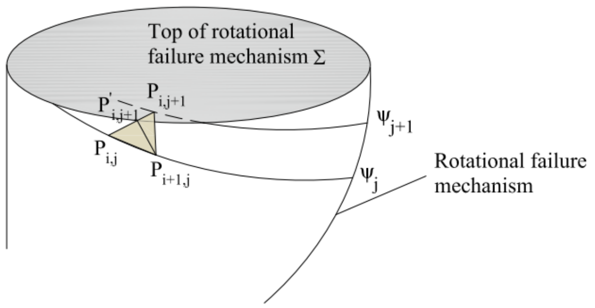

Fig. 5 A special produce of point generation, if points $P_{i,j}$ and $P_{i+1,j}$ are below, and $P_{i,j+1}$ is above the top face of the rotational failure mechanism

mechanism of this paper in single layer is bounded by only one log-spiral emerging from point *B*, which is different from other works (Ibrahim *et al.* 2015, Pan and Dias 2017a, Pan and Dias 2017b) bounded by two log-spirals emerging from points *A* and *B* (see Fig. 1). The equation of the log-spiral emerging from point *B* in a polar (*r*, *β*) coordinate system is as follows

$$r = r_B e^{(\beta_B - \beta)\tan\varphi} \tag{1}$$

where the meanings of r_B and and β_B can be easily identified in Fig. 1(b). φ is the friction angle of the soil of single layer. Having drawn longitude section of the new collapse analysis model (see Fig. 1(b)), construction plans of Section 1 and Section 2 are defined by using spatial discretization technique (Mollon *et al.* 2011). Firstly, the counter of the tunnel face is uniformly discretized by n points (see Fig. 2a), and the moving block of Section 1 and Section 2 is then discretized by a series of planes with the same point *O* (see Fig. 2b). For Section 1, the discrete plane ψ_j is the one which pass through point *O* and two symmetric discrete points of tunnel face. In contrast to Section 1, the discrete plane ψ_j of Section 2 is generated by the former plane ψ_{j-1} rotating around a horizontal X-axis passing through point *O* with a constant angular δ_β. Once the construction plans are defined, the 3D rotational failure mechanism will be generated by "point by point" method. As shown in Fig. 3, the point $P_{i,j+1}$ of plane ψ_{j+1} is generated by the given points $P_{i,j}$ and $P_{i+1,j}$ of plane ψ_j by respecting normality condition (Chen 1975). And the surface $\Sigma_{i,j}$ is linked by the given point $P_{i,j}$ and $P_{i+1,j}$ and the created point $P_{i,j+1}$. Consequently, the elementary volumes $V_{i,j}$ is defined by the projection of the obtained external facets $\Sigma_{i,j}$ on the central plane (*Y,Z*). Notice that the sign *i* denotes a point in the given plane *j*. For a more detailed process of the discretization scheme and the point generation procedures can refer Mollon *et al.* (2011).

However, in the practical engineering, the properties of the soil (soil weight γ, internal friction angle φ and cohesion *c*) would not remain constant with the increasing of soil depth (Ibrahim *et al.* 2015, Tang *et al.* 2014). Therefore the new collapse mechanism proposed in this study would actually consider the effect of layered soils on the stability of tunnel face. For the sake of simplicity, the rotational failure mechanism is extended to two layers with horizontal intersecting. And in this study, according to the location of the intersecting of two layers, the distribution of soil layer can be divided into two cases i) interface is in the crossed layer (see Fig. 4) and ii) interface is in the cover layer (see Fig. 7).

As shown in Fig. 3, when the intersection locates in the crossed layer, the shape of the rotational failure mechanism would be obviously different with the case of single layer for the reason that any differential surface of the rotational failure mechanism must respect the normality condition (Chen 1975) which indicates that the normal vector of the differential surface should make an angle $\pi/2+\varphi$ with the velocity vector. Notice that the longitudinal section of rotational failure mechanism is bounded by two log-spirals emerging from *B* and *JB* in two crossed layers. And both of them rotate around the same horizontal X-axis passing through point *O* with a constant angular velocity ω. The expression of the log-spirals of longitude section emerging from *B* and *JB* in a polar (*r, β*) coordinate system are given as follows

$$r = r_B e^{(\beta_B - \beta)\tan\varphi_1} \left(\beta_B \le \beta \le \beta_{JB}\right) \tag{2}$$

$$r = r_{JB} e^{(\beta_{JB} - \beta)\tan\varphi_2} \left(\beta_{JB} < \beta \le \beta_{JA}\right) \tag{3}$$

where r_B, β_B, r_{JB}, β_{JB} and β_{JA} can be easily identified in Fig. 4. In addition, φ_1 and φ_2 are the friction angles of lower and upper soil of crossed layer, respectively. Moreover, as shown in Fig. 7, when the interface is in the cover layer, the feature of the failure mechanism is consistent with the single layer.

Note that the procedures of the generation of 3D rotational failure mechanism for layered soils are consistent with the case of single layer. For the new collapse failure mechanism in this study, the closure of the rotational failure mechanism must fulfill the following two conditions: i) the angle of the next plane β_{j+1} is bigger than β_{JA} (see Fig. 1(b)) and ii) any point in plane ψ_{j+1} is above the top of the rotational failure mechanism (Plane *Z*=0) adjacent to the tunnel face. Notice that if points $P_{i,j}$ and $P_{i+1,j}$ are both above the top of the rotational failure mechanism (Plane *Z*=0), point $P_{i,j+1}$ does not exist. And if points $P_{i,j}$ and $P_{i+1,j}$ are both below the top of the rotational failure mechanism (Plane *Z*=0), point $P_{i,j+1}$ is generated by the method of "point by point". However, if points $P_{i,j}$ is below, and $P_{i,j+1}$ is above the top of the rotational failure mechanism (Plane *Z*=0), points $P_{i,j+1}$ is substituted by the intersection ($P`_{i,j+1}$) between the segment connected by two points $P_{i,j+1}$ and $P_{i,j}$ and the top of the rotational failure mechanism (Plane *Z*=0) by using linear interpolation (see Fig. 5).

2.2 Generation of pressure arch

The detailed procedure of the calculation of pressure arch is introduced in this section. In this paper, the pressure arch effect is treated as a uniformly distributed force that is calculated by the Terzaghi earth theory (see Fig. 7), which indicates that the intersection Σ of the rotational failure mechanism and the (*X,Z*) plane (see Fig. 1(b)) is essential to be obtained firstly (Zhang *et al.* 2015). The intersection Σ is derived by employing the linear interpolation method. The

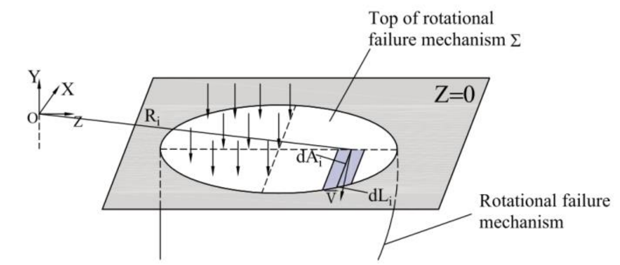

Fig. 6 The top of the rotational failure mechanism

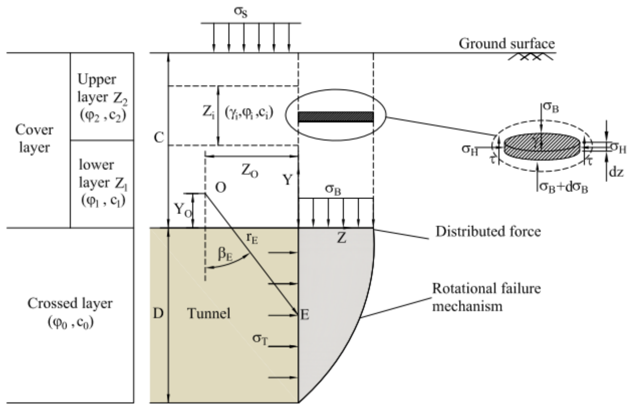

Fig. 7 Distributed force calculated by Terzaghi earth theory

details are as follows:

Assuming that the Eq. (4) holds, that is, the two given points $P_{i,j}$ and $P_{i+1,j}$ are both below the top of the rotational failure mechanism and the generated points $P_{i,j+1}$ is above the intersection Σ.

$$\begin{cases} Y_{i,j} \cdot Y_{i,j+1} < 0 \\ Y_{i+1,j} \cdot Y_{i,j+1} < 0 \end{cases} \tag{4}$$

where $Y_{i,j}$,$Y_{i+1,j}$, and $Y_{i,j+1}$ are given as follows

$$P(i,j) = \left[X_{i,j}, Y_{i,j}, Z_{i,j}\right] \tag{5}$$

$$P(i+1,j) = \left[X_{i+1,j}, Y_{i+1,j}, Z_{i+1,j}\right] \tag{6}$$

$$P(i,j+1) = \left[X_{i,j+1}, Y_{i,j+1}, Z_{i,j+1}\right] \tag{7}$$

Or Eq. (8) is established, that is, points $P_{i,j}$ is below, $P_{i+\mathrm{d},j}$ is above the top of the rotational failure mechanism and the generated points $P_{i,j+1}$ is above the intersection Σ.

$$\begin{cases} Y_{i,j} \cdot Y_{i,j+1} < 0 \\ Y_{i+1,j} \cdot Y_{i,j+1} > 0 \end{cases} \tag{8}$$

The expression of the equation of space straight line L_j (see Eq. (9)) can be easily obtained by combining Eq. (5) and Eq. (7).

$$L_j : \frac{x - X_{i,j}}{X_{i,j+1} - X_{i,j}} = \frac{y - Y_{i,j}}{Y_{i,j+1} - Y_{i,j}} = \frac{z - Z_{i,j}}{Z_{i,j+1} - Z_{i,j}} \tag{9}$$

Then we can obtain one point $K(i)$ of the intersection Σ by combining Eq. (9) and (X,Z) plane (see Eq. (10)).

$$K(i) = \left[x_i, y_i, z_i\right] \tag{10}$$

where x_i, y_i and z_i are given as follows

$$\begin{cases} x_i = -\dfrac{\left(X_{i,j+1} - X_{i,j}\right)Y_{i,j}}{Y_{i,j+1} - Y_{i,j}} + X_{i,j} \\ y_i = 0 \\ x_i = -\dfrac{\left(Y_{i,j+1} - Y_{i,j}\right)Y_{i,j}}{Y_{i,j+1} - Y_{i,j}} + Z_{i,j} \end{cases} \tag{11}$$

By employing Eqs. (4)-(11), we can obtain a series of points representing the boundary of the intersection Σ. Notice that the intersection Σ is symmetrical about (Y,Z) plane (see Fig. 6).

Fig. 6 shows that the calculation of the area A and perimeter L can be derived by the summation of elementary area dA and elementary perimeter dL as follows

$$A = \sum_i dA_i \tag{12}$$

$$L = \sum_i dL_i \tag{13}$$

where dA_i and dL_i can be easily identified from Fig. 6.

Having drawn the intersection Σ, the uniformly distributed force can be calculated by using Terzaghi earth theory (see Fig. 7). And due to the presence of soil arching effect, the value of the distributed force is not more than the soil weight above the intersection Σ. The details are as follows:

Presuming that the soil is homogeneous and meets the Mohr-Coulomb failure criterion. As shown in Fig 6, the vertical equilibrium of an infinitesimal layer dz at depth z and limit condition at the ground surface are as follows

$$\begin{cases} A\sigma_B + A\gamma dz = A\left(\sigma_B + d\sigma_B\right) + L\tau dz \\ \tau = c + \sigma_H \tan\varphi = c + K_0 \sigma_B \tan\varphi \\ z = 0 \,|\, \sigma_B = \sigma_S \end{cases} \tag{14}$$

where K_0 is the lateral pressure coefficient. Anagnostou and Kovári (1996) is referred to calculate the lateral pressure coefficient K_0 in this paper.

The value of the vertical stress σ_B of an infinitesimal layer dz at depth z can be calculated by using Eq. (14) as follows

$$\sigma_B = \frac{A\gamma - Lc}{LK_0 \tan\varphi}\left(1 - e^{-\frac{LK_0 \tan\varphi}{A} z}\right) + \sigma_S e^{-\frac{LK_0 \tan\varphi}{A} z} \tag{15}$$

Notice that the vertical stress σ_B should less than the total soil weight of cover layer for the presence of arching effect.

$$\begin{aligned} \sigma_B = {} & \frac{A\gamma - Lc}{LK_0 \tan\varphi}\left(1 - e^{-\frac{LK_0 \tan\varphi}{A} z}\right) + \sigma_S e^{-\frac{LK_0 \tan\varphi}{A} z} \\ & \le \sum_{i=1}^{N} \gamma_i z_i + \sigma_T \end{aligned} \tag{16}$$

Assuming the cover layer is composed of N layers of different soil properties, and therefore the calculation of vertical stress p_i of layer z_i can be obtained from Eq. (15) as follows

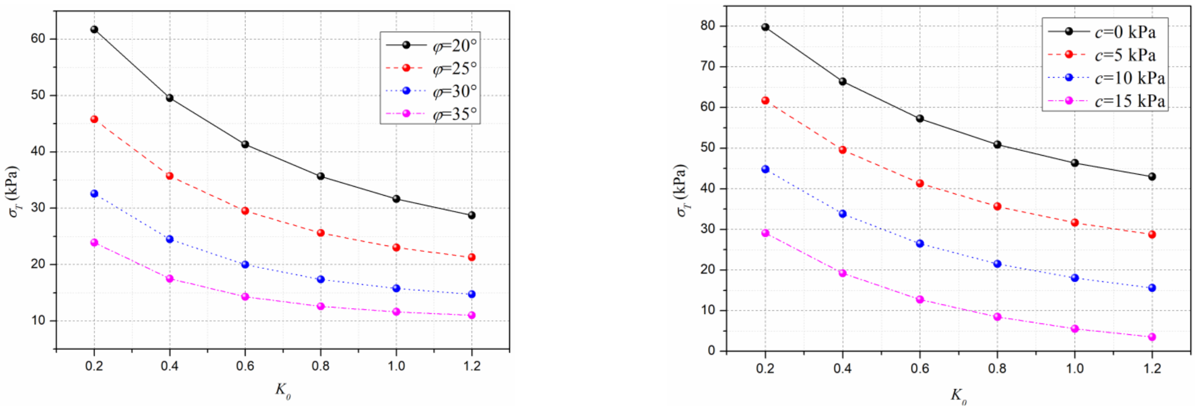

(a) c= 5kPa (b) φ=20°

Fig. 8 Influence of the lateral stress ratio K_0 on the limit support pressures

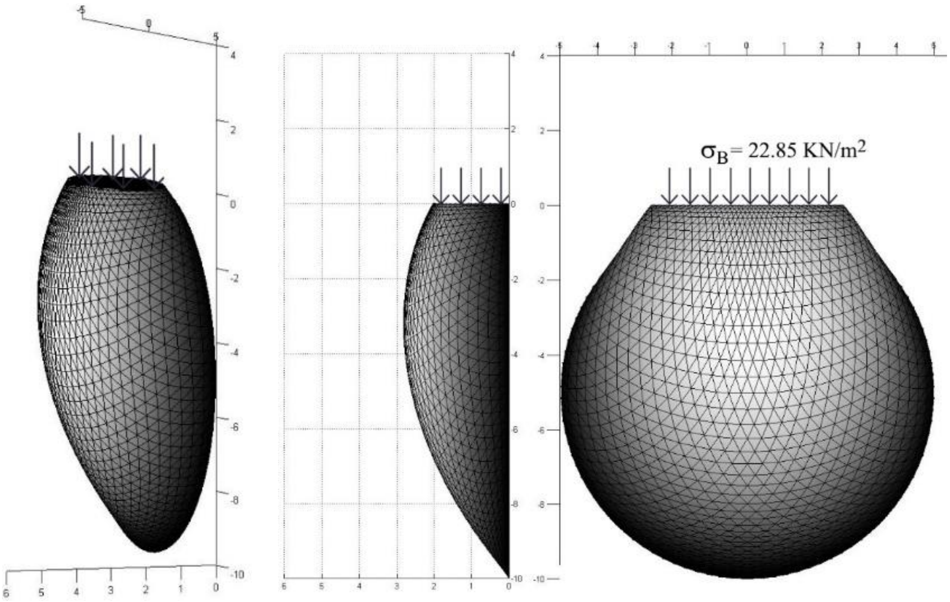

Fig. 9 View of the new 3D collapse failure mechanisms in single layer when D=10 m, γ=20 kN/m^3, φ=35° and c=0 kPa

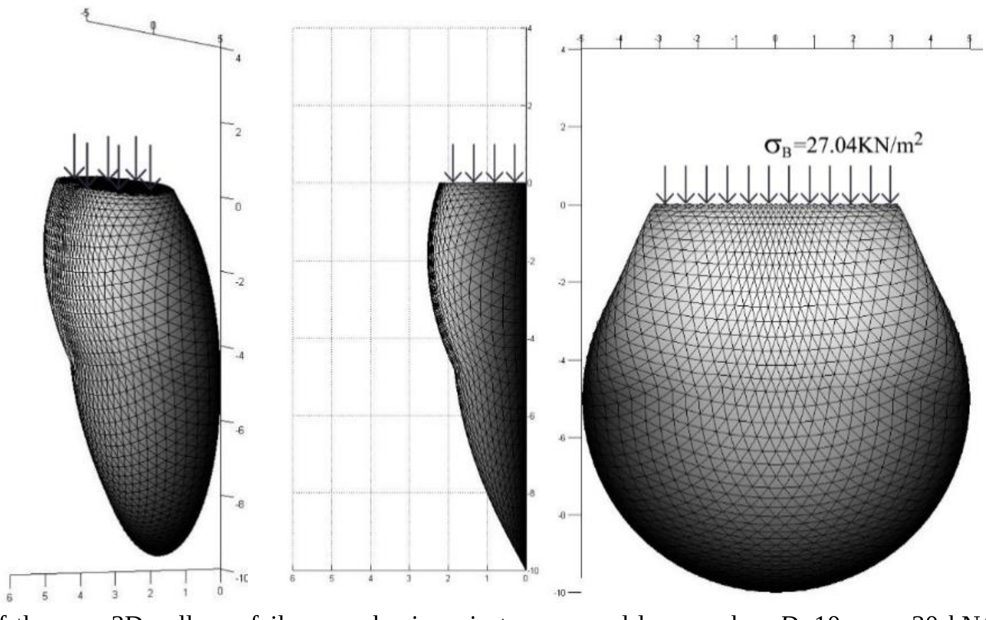

Fig. 10 View of the new 3D collapse failure mechanisms in two crossed layers when D=10 m, γ=20 kN/m^3, φ_1=35°, φ_0 =φ_2=30°, c_0=c_1=c_2=0 kPa, and U=0.45

$$P_i=\frac{A\gamma_i}{LK_{0i}\tan\varphi_i}\left(1-e^{-\frac{LK_{0i}\tan\varphi_i}{A}z_i}\right)-\frac{c}{K_{0i}\tan\varphi_i}\left(1-e^{-\frac{LK_{0i}\tan\varphi_i}{A}z_i}\right) \tag{17}$$
$$+p_{i-1}e^{-\frac{LK_{0i}\tan\varphi_i}{A}z_i}\;(i=1,\ldots,n)$$

where $p_0=\sigma_s$, $p_n=\sigma_B$ and K_{0i} is the lateral pressure coefficient.

By employing recursive relationship of Eq. (17), the distributed force σ_B can be derived as follows

$$\begin{aligned}\sigma_B&=\frac{A\gamma_n}{LK_{0n}\tan\varphi_n}\left(1-e^{-\frac{LK_{0n}\tan\varphi_n}{A}z_n}\right)\\&+\sum_{k=1}^{n-1}\left[\frac{A\gamma_k}{LK_{0k}\tan\varphi_k}\left(1-e^{-\frac{LK_{0k}\tan\varphi_k}{A}z_k}\right)\prod_{m=k+1}^{n}e^{-\frac{LK_{0m}\tan\varphi_m}{A}z_m}\right]\\&-\frac{c_n}{K_{0n}\tan\varphi_n}\left(1-e^{-\frac{LK_{0n}\tan\varphi_n}{A}z_n}\right)\\&-\sum_{k=1}^{n-1}\left[\frac{c_k}{K_{0k}\tan\varphi_k}\left(1-e^{-\frac{LK_{0k}\tan\varphi_k}{A}z_k}\right)\prod_{m=k+1}^{n}e^{-\frac{LK_{0m}\tan\varphi_m}{A}z_m}\right]\\&+\sigma_S\prod_{i=1}^{n}e^{-\frac{LK_{0i}\tan\varphi_i}{A}z_i}\end{aligned} \tag{18}$$

In order to determine the value of the the lateral stress ratio K_0 (see Eqs. (14)-(18)), the effect of the lateral stress ratio K_0 on the critical support pressures is presented in Fig. 8 based on the improved failure model proposed by this study with the cases of D=10 m, C/D=2.0, γ=18 kN/m^3 and c=5 kPa or φ=20°. As shown in Fig. 8, the critical support pressure decreases as the lateral stress ratio K_0 increases, which indicates that the the lateral stress ratio K_0 has a greatly significant influence on the stability of tunnel face. To simplify the calculation of limit support pressure, an empirical constant (K_0=0.8) (Anagnostou and Kovári 1996) is adopted to investigate the tunnel face stability issue in this study.

3. Work rate calculations

Figs. 9 and 10 show the new 3D collapse failure model considering the soil weight of cover layer as uniformly distributed force on the rotational failure mechanism in single and layered soils ($U=Z_1/D$ (see Fig. 4)), respectively. The external rate of work is composed of three parts: i) work rate of support pressures, ii) work rate of distributed force acting on the rotational failure mechanism and iii) work rate of soil weight. For the internal dissipation, it occurred along the velocity discontinuity face. The details are as follows:

(1) Rate of external work

(a) The work of support pressures

$$W_{\sigma_T}=\iint_{\Sigma}\sigma_T\, v dS=\sum_j\left(\sigma_T\, v_j\,\Sigma_j\right)=\omega\sigma_T\sum_j\left(\Sigma_j\cdot R_j\cos\beta_j\right) \tag{19}$$

(b) The work rate of distributed force acting on the rotational failure mechanism

$$W_{\sigma_B}=\iint_{\Sigma^{`}}\sigma_B\, v dS=\sum_l\left(\sigma_B\, v_l\,\Sigma_l^{`}\right)=\omega\sigma_B\sum_l\left(\Sigma_l^{`}\cdot R_l\sin\beta_l\right) \tag{20}$$

(c) The work rate of soil weight

$$\begin{aligned}W_\gamma&=\iiint_V\gamma v dV=\sum_j\left(\gamma_j\cdot v_{i,j}\cdot V_{i,j}+\gamma_j\cdot v_{i,j}^{'}\cdot V_{i,j}^{'}\right)\\&=\omega\gamma\sum_{i,j}\left(R_{i,j}V_{i,j}\sin\beta_{i,j}+R_{i,j}^{`}V_{i,j}^{`}\sin\beta_{i,j}^{'}\right)\end{aligned} \tag{21}$$

(2) Rate of internal dissipation

$$W_D=\iint_S cv\cos\varphi dS=\omega c\cos\varphi\sum_{i,j}\left(R_{i,j}S_{i,j}+R_{i,j}^{`}S_{i,j}^{`}\right) \tag{22}$$

(3) Calculation of the critical support pressure

According to the displacement boundary condition of kinematically admissible velocity field, the limit support pressure can be calculated by equating the total rate of work done by external force and the total rate of work of energy dissipation as follows

$$\sigma_T=\max_{\left(\frac{r_E}{D},\beta_E\right)}\left\lfloor\gamma\cdot D\cdot N_\gamma-c\cdot N_c+\sigma_B\cdot N_B\right\rfloor \tag{23}$$

where N_γ, N_c and N_B respectively represent the effect of soil weight, coefficient and distributed force acting on the top of rotational failure mechanism and can be calculated by Eqs. (24)-(26)

$$N_\gamma=\frac{\sum_{i,j}\left(V_{i,j}R_{i,j}\sin\beta_{i,j}+V_{i,j}^{`}R_{i,j}^{`}\sin\beta_{i,j}^{`}\right)}{D\sum_j\left(\Sigma_j\, R_j\cos\beta_j\right)} \tag{24}$$

$$N_c=\frac{\cos\varphi_j\sum_{i,j}\left(R_{i,j}S_{i,j}+R_{i,j}^{`}S_{i,j}^{`}\right)}{D\sum_j\left(\Sigma_j\, R_j\cos\beta_j\right)} \tag{25}$$

$$N_B=\frac{\sum_l\left(\Sigma_l^{`}\, R_l\sin\beta_l\right)}{\sum_j\left(\Sigma_j\, R_j\cos\beta_j\right)} \tag{26}$$

Note that the limit support pressure σ_T is the maximum of the Eq. (23) by employing all possible geometric parameters r_E/D and β_E, which is implemented by using the unconstrained optimization tool (fiminsearch) of Matlab.

4. Comparison with existing approaches

The results derived from the new collapse failure mechanism proposed in this study were validated by comparing with those from Han *et al.* (2016) and Senent and Jimenze (2015) which are all based on the same limit analysis methods. The detailed analysis parameters of soil are shown in Table 1.

4.1 Influence of the crossed layer on limit support pressure

4.1.1 Single crossed layer

In this subsection, the cover layer is regarded as a single layer with constant soil properties (γ_1, c_1 and φ_1) and a single crossed layer with varying soil properties (γ_0, c_0 and φ_0). Figs. 11 and 12 respectively show the curves of the

Table 1 Selection of parameters

Sets' number	Layers' name	(KN/m^3)	D(m)	C/D	φ(°)	c(kPa)
1	Cover layer	18	6	1.5	20	2.5
	Crossed layer				15~35	1.5~4.5
2	Cover layer	18	10	1.5	φ_0=20	c_0=2.5
	Crossed layer				φ_1=15	c_1=2.5
					φ_2=10	c_2=2.5
3	Cover layer	18	6	1.5	15~35	1.5~4.5
	Crossed layer				20	2.5
4	Cover layer	20	6	1.5	φ_2=45	c_2=0
					φ_1=15	c_1=5
	Crossed layer				φ_0=15	c_0=5

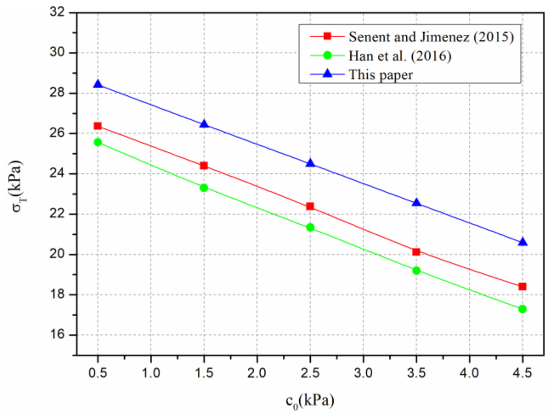

(a) φ_0=20°

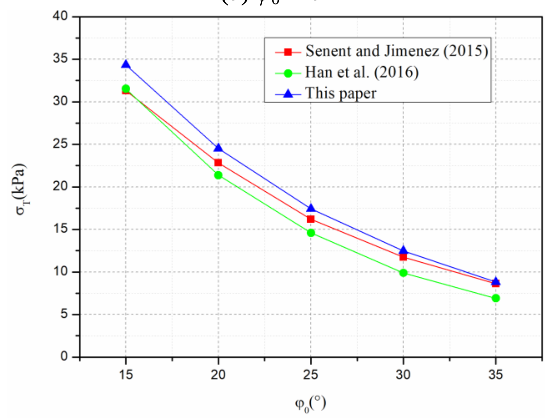

(b) c_0=2.5 kPa

Fig. 11 Influence of single crossed layer on the limit support pressures

values of limit support pressures with the variation of the parameters c_0 and φ_0.

In Fig. 11(a), the limit support pressures decrease linearly from 28.42 kPa to 20.59 kPa with the increasing of c_0 from 0.5kPa to 4.5kPa. However, with the variation of φ_0 from 15° to 35° in Fig. 11(b), the limit support pressures decrease nonlinearly from 34.32 kPa to 8.81 kPa. And the descent amount of the limit support pressures also declines with the same increasing amount of φ_0 in Fig. 11, which indicates that the limit support pressures are more sensitive to the low friction angle. This observation is consistent with

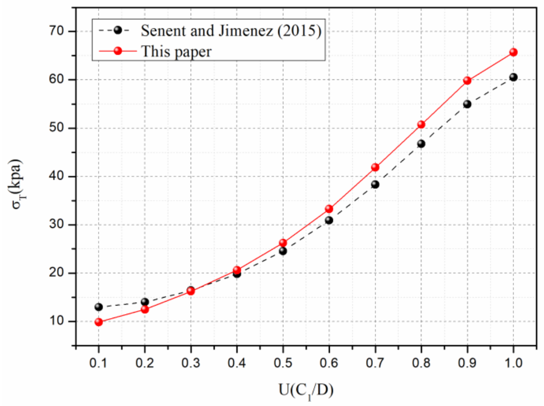

Fig. 12 Variation of U on limit support pressure (U=Z_1/D)

existing researches (Han *et al.* 2016, Senent and Jimenez 2015) based on same limit analysis methods. Note that Figs. 11(a) and 11(b) show that results provided by this study is slightly higher than those from Sentent and Jimenez (2015) and Han *et al.* (2016). In the framework of limit analysis theory, due to the critical support pressures are derived by equating the rate of external work done by the external forces to the internal rate of energy dissipation along the velocity discontinuity face, so the results obtained from the limit analysis theory are unsafe to resist to limit load. In other words, the critical support pressures provided by kinematically admissible failure mechanism are smaller than the exact one (Ibrahim *et al.* 2015, Pan and Dias 2016b). Therefore, we can conclude that the strict lower bound of limit support pressure provided by Sentent and Jimenez (2015) is greatly improved by the developed model of this paper, which indicates that the advanced mechanism proposed in this paper can provide much safer estimation values of required limit support pressures.

4.1.2 Two crossed layers

The second set of analysis describes the cases of two crossed layers with the constant upper crossed layer, lower crossed layer and cover layer strength parameters (see Table 1). Fig 12 shows that the curves of the limit support pressures with the variation of relative thickness U (U=Z_1/D (see Fig. 4)).

As shown in Fig. 12, the results obtained from this paper increase from 9.86kPa to 65.68kPa with the increasing of relative thickness U from 0.1 to 1.0. Notice that, when U is < 0.6, the variation values of limit support pressure keep increasing, however, when U reaches 0.6, the variation values of limit support pressure gradually reduce with the same increasing amount of relative thickness U, which indicates that the limit support pressures are remarkably influenced by the lower layer. And this observation is consistent with the results provided by Senent and Jimenez (2015). Moreover, when U is < 0.3, the results obtained from this paper is slightly smaller than Senent and Jimenez (2015), but after U is > 0.3, the situation is reverse in Fig. 12. The observation indicates that the limit support pressures obtained from the new failure mechanism are greatly influenced by lower layer compared with those of Senent and Jimenez (2015).

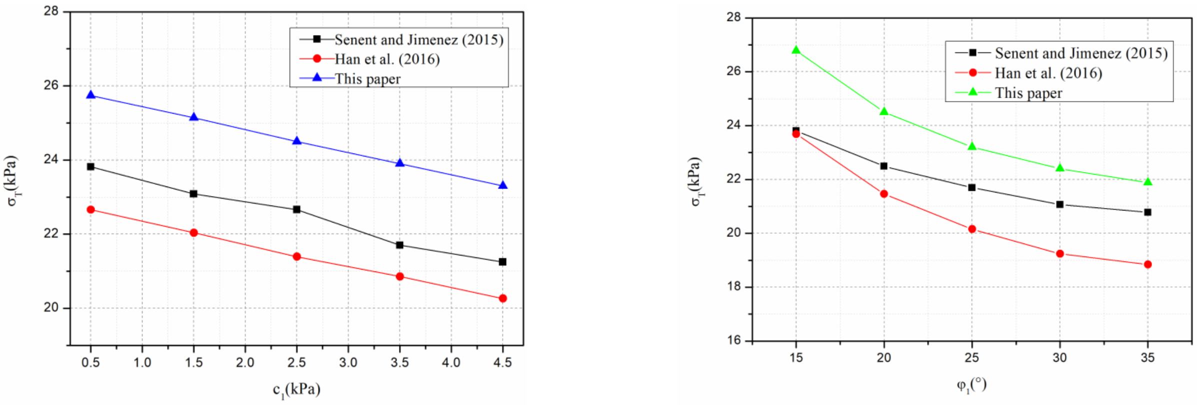

(a) φ_1=20° (b) c_1=2.5 kPa

Fig. 13 Influence of single cover layer on the limit support pressure

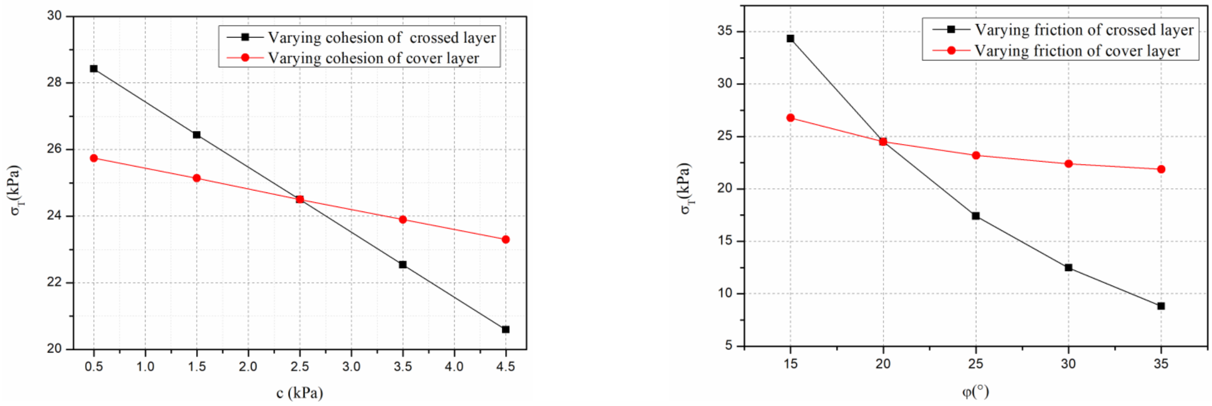

(a) φ=20° (b) c=2.5 kPa

Fig. 14 Comparison of influence of crossed and cover layer on limit support pressure

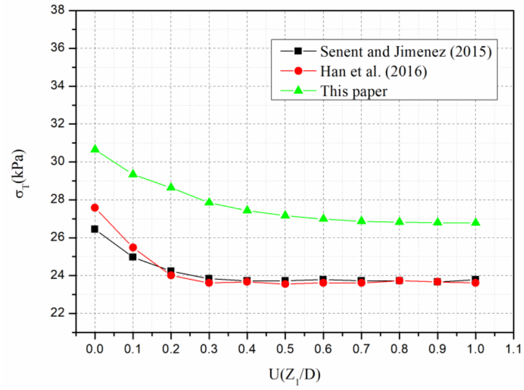

Fig. 15 Variation of U on limit support pressure (U=Z_1/D)

4.2 Influence of the cover layer on limit support pressure

4.2.1 Single cover layer

In this section, a reverse situation compared with the first set of analyses is analyzed to investigate the limit support pressures, which describe the case of a single crossed layer with constant soil properties (γ_0, c_0 and φ_0) and a single cover layer with varying soil properties (γ_1, c_1 and φ_1). Figs. 13(a) and 13(b) present the curves of limit support pressure with the variation of c_1 and φ_1, respectively.

Fig. 13(a) shows that the limit support pressures decrease linearly from 25.74 kPa to 23.3 kPa as the c_1 increase from 0.5 kPa to 4.5 kPa, whereas the limit support pressures drop non-linearly from 26.78 kPa to 21.88 kPa with the increase of φ_1 from 15° to 35° in Fig. 13(b). Similarly, Figs. 13(a) and 13(b) both presents that the results obtained from this paper are higher than those provided by Senent and Jimenez (2015) and Han *et al.* (2016).

In addition, for this section is a reserve situation compared with the first set of analyses, it is essential to compare the sensitivity of the soil properties of crossed and cover layer on limit support pressures. Figs. 14(a) and 14(b) show the curves of the influence of cohesion and internal friction angle of crossed and cover layer on the limit support pressures, respectively. As shown in Fig. 14(a), with the variation of cohesion of crossed and cover layer from 0.5 kPa to 3.5 kPa, the decrements of limit support pressure respectively equal 7.83 kPa and 2.44 kPa. And with the variation of friction of crossed and cover layer from 15° to 35°, the decrements of limit support pressure respectively equal 25.51 kPa and 4.9 kPa in Fig. 14(b). Those observations indicate that the limit support pressures are greatly influenced by the soil properties of crossed layer, which is also derived by Senent and Jimenez (2015) and Han *et al.* (2016).

4.2.2 Two cover layers

In this section, assuming that the cover layer is composed of two layers of different soil properties and the crossed layer with the constant soil properties (Table 1). Fig. 15 shows the influence of relative thickness U ($U=Z_1/D$ (see Fig. 7)) on the limit support pressures.

As shown in Fig. 15, when relative thickness U is less than 0.5, the results provided by this paper and other researches (Han *et al.* 2016, Senent and Jimenze 2015) are slightly impacted by the variation of relative thickness U. However, once the relative thickness U is bigger than 0.5, the limit support pressures would keep constant and is no longer influenced by the relative thickness U, which indicates the presence of soil arching effect.

5. Conclusions

This paper proposes a new collapse failure mechanism which is composed of the rotational failure mechanism adjacent to the tunnel face and a uniformly distributed force acting on the top of the rotational failure mechanism to analyze the stability of tunnel face by using kinematic approach of limit analysis theory. The classical Terzaghi earth theory is used to calculate the uniformly distributed force acting on the top of the rotational failure mechanism. Note that the top of the rotational failure mechanism is calculated by employing method of linear interpolation in this paper. Then the results from this paper are compared with Han *et al.* (2016) and Senent and Jimenze (2015). The main conclusions are as follows:

- The limit support pressure obtained from this paper is an improving of rigorous bound compared with existing works which are based on the same limit analysis.
- The parameters of crossed layer have a greater influence than the cover layer on the limit support pressure with the same variable range of the soil properties.
- When the crossed is two layers, the varying values of limit support pressures increase first and then decrease, which illustrates that the limit support pressure is greater influenced by the lower layer.
- When the cover is two layers, limit support pressure decreases first and then nearly remains constant with the increasing of relative thickness U, which indicates that the presence of soil arching effect.

Even though the results of experiment and numerical methods about the collapse failure feature, that is a shear failure band occurs in the lower part and a pressure arch happens at the upper part, and the spatial discretization technology are considered to investigate the stability of the tunnel face, a possible extension is to analyze the face stability of shield tunnel for the presence of face reinforced (Zou and Zhang 2019c), possible seismic load (Peng *et al.* 2018, Zhao *et al.* 2018) or anisotropic and nonhomogeneous soils (Li and Zou 2019), because the model is created by using spatial discretization and "point by point" scheme with a specified boundary condition.

References

Anagnostou, G. and Kovári, K. (1996), "Face stability conditions with earth-pressure-balanced shields", *Tunn. Undergr. Sp. Technol.*, **11**(2), 165-173.

Anagnostou, S.T.G. (2012), "The contribution of horizontal arching to tunnel face stability", *Geotechnik*, **35**(1), 34-44.

Anagnostou, G. and Perazzelli, P. (2013), "The stability of a tunnel face with a free span and a non-uniform support", *Geotechnik*, **36**(1), 40-50.

Broere, W. (2001), "Tunnel face stability & new CPT applications", Ph.D. Dissertation, Delft University of Technology, Delft, The Netherlands.

Chen, W.F. (1975), *Limit Analysis and Soil Plasticity*, *Elsevier*, Amsterdam, The Netherlands.

Chambon, P. and Corté, J.F. (1994), "Shallow tunnels in cohesionless soil: Stability of tunnel face", *Geotech. Eng.*, **120**(7), 1148-1165.

Chen, R.P., Tang, L.J. and Ling, D.S. (2011), "Face stability analysis of shallow shield tunnels in dry sandy ground using the discrete element method", *Comput. Geotech.*, **38**(2), 187-195.

Chen, R.P., Li, J. and Kong, L.G. (2013), "Experimental study on face instability of shield tunnel in sand", *Tunn. Undergr. Sp. Technol. Incorp. Trenchless Technol. Res.*, **33**(1), 12-21.

Chen, R.P., Tang, L.J., Yin, X.S., Chen, Y.M. and Bian, X.C. (2015), "An improved 3D wedge-prism model for the face stability analysis of the shield tunnel in cohesionless soils", *Acta Geotech.*, **10**(5), 683-692.

Horn, N. (1961), "Horizontal earth pressure on the vertical surfaces of the tunnel tubes", *Proceedings of the National Conference of the Hungarian Civil Engineering Industry*, Budapest, Hungary, November.

Han, K., Zhang, C. and Zhang, D. (2016), "Upper-bound solutions for the face stability of a shield tunnel in multilayered cohesive-frictional soils", *Comput. Geotech.*, **79**, 1-9.

Idinger, G., Aklik, P. and Wu, W. (2011), "Centrifuge model test on the face stability of shallow tunnel", *Acta Geotech.*, **6**(2), 105-117.

Ibrahim, E., Soubra, A.H. and Mollon, G. (2015), "Three-dimensional face stability analysis of pressurized tunnels driven in a multilayered purely frictional medium", *Tunn. Undergr. Sp. Technol.*, **49**(1), 18-34.

Krause, T. (1987), "Schildvortrieb mit flüssigkeits-und erdgestützter ortsbrust", Technical University Carolo-Wilhelmina, Brunswick, Germany.

Kirsch, A. (2010), "Experimental investigation of the face stability of shallow tunnels in sand", *Acta Geotech.*, **5**(1), 43-62.

Khezri, N., Mohamad, H. and Fatahi, B. (2016), "Stability assessment of tunnel face in a layered soil using upper bound theorem of limit analysis", *Geomech. Eng.*, **11**(4), 471-492.

Leca, E. and Dormieux, L. (1990), "Upper and lower bound solutions for the face stability of shallow circular tunnels in frictional material", *Géotechnique*, **40**(4), 581-606.

Li, C. and Zou, J.F. (2019), "Closed-form solution for undrained cavity expansion in anisotropic soil mass based on the spatially mobilized plane failure criterion", *Int. J. Geomech.*, Accepted.

Mollon, G., Dias, D. and Soubra, A.H. (2009), "Probabilistic Analysis and Design of Circular Tunnels against Face Stability", *Int. J. Geomech.*, **9**(6), 237-249.

Mollon, G., Dias, D. and Soubra, A.H. (2010), "Face stability analysis of circular tunnels driven by a pressurized shield", *J. Geotech. Geoenviron. Eng.*, **136**(1), 215-229.

Mollon, G., Daniel, D. and Abdul-Hamid, S. (2011), "Rotational failure mechanisms for the face stability analysis of tunnels driven by a pressurized shield", *Int. J. Numer. Anal. Meth. Geomech.*, **35**(12), 1363-1388.

Oreste, P.P. and Dias, D. (2012), "Stabilisation of the excavation face in shallow tunnels using fibreglass dowels", *Rock Mech. Rock Eng.*, **45**(4), 499-517.

Pan, Q. and Dias, D. (2016a), "Face stability analysis for a shield-driven tunnel in anisotropic and nonhomogeneous soils by the kinematical approach", *Int. J. Geomech.*, **16**(3), 04015076.

Pan, Q. and Dias, D. (2016b), “The effect of pore water pressure on tunnel face stability”, *Int. J. Numer. Anal. Meth. Geomech.*, **40**(15), 2123-2136.

Pan, Q. and Dias, D. (2017a), “Upper-bound analysis on the face stability of a non-circular tunnel”, *Tunn. Undergr. Sp. Technol.*, **62**, 96-102.

Pan, Q. and Dias, D. (2017b), “Safety factor assessment of a tunnel face reinforced by horizontal dowels”, *Eng. Struct.*, **142**, 56-66.

Peng, X., Yu, P. and Zhang, Y. (2018), “Applying modified discontinuous deformation analysis to assess the dynamic response of sites containing discontinuities”, *Eng. Geol.*, **246**, 349-360.

Soubra, A.H. (2000), “Kinematical approach to the face stability analysis of shallow circular tunnels”, *Proceedings of the 8th International Symposium on Plasticity*, Vancouver, Canada, July.

Schuller, H. and Schweiger, H.F. (2002), “Application of a multilaminate model to simulation of shear band formation in NATM-tunnelling”, *Comput. Geotech.*, **29**(7), 501-524.

Subrin, D. and Wong, H. (2002), “Tunnel face stability in frictional material: A new 3D failure mechanism”, *Comptes Rendus Mecanique*, **330**(7), 513-519.

Senent, S. and Jimenez, R. (2015), “A tunnel face failure mechanism for layered ground, considering the possibility of partial collapse”, *Tunn. Undergr. Sp. Technol.*, **47**, 182-192.

Tang, X.W., Liu, W. and Albers, B. (2014), “Upper bound analysis of tunnel face stability in layered soils”, *Acta Geotech.*, **9**(4), 661-671.

Vermeer, P.A., Ruse, N. and Marcher, T. (2002), “Tunnel heading stability in drained ground”, *Felsbau*, **20**(6), 8-18.

Yang, X.L. and Yan, R.M. (2015), “Collapse mechanism for deep tunnel subjected to seepage force in layered soils”, *Geomech. Eng.*, **8**(5), 741-756.

Yang, X.L., Xu, J.S. and Li, Y.X. (2016), “Collapse mechanism of tunnel roof considering joined influences of nonlinearity and non-associated flow rule”, *Geomech. Eng.*, **10**(1), 21-35.

Zhang, C., Han, K. and Zhang, D. (2015), “Face stability analysis of shallow circular tunnels in cohesive-frictional soils”, *Tunn. Undergr. Sp. Technol.*, **50**, 345-357.

Zhao, L.H., Cheng, X., Li, D.J. and Zhang, Y.B. (2018), “Influence of non-dimensional strength parameters on seismic stability of cracked slopes”, *J. Mountain Sci*.

Zou, J.F., Qian, Z.H., Xiang, X. and Chen, G.H. (2019a), “Face stability of a tunnel excavated in saturated nonhomogeneous soils”, *Tunn. Undergr. Sp. Technol.*, **83**, 1-17.

Zou, J.F., Chen, G.H. and Qian, Z.H. (2019b), “Tunnel face stability in cohesion-frictional soils considering the soil arching effect by improved failure models”, *Comput. Geotech.*, **106**, 1-17.

Zou, J.F. and Zhang, P.H. (2019c), “Analytical model of fully grouted bolts in pull-out tests and in situ rock masses”, *Int. J. Rock Mech. Min. Sci.*, **113**, 278-294.

Zou, J.F., Liu, L. and Xia, M.Y. (2019d), “A new simple approach for the quasi-plane strain problem of circular tunnel in strain-softening rock mass incorporating the effect of out-of-plane stress”, *Acta Geotech.*, In Press.

GC